Broadband Combustion Noise Simulation of the PRECCINSTA Burner based on Stochastic Sound Sources

Felix Grimm, Duncan Ohno, Berthold Noll, Manfred Aigner
Institute of Combustion Technology
German Aerospace Center (DLR)
Pfaffenwaldring 38-40
70569 Stuttgart, Germany
Email: felix.grimm@dlr.de

Roland Ewert, Jürgen Dierke
Institute of Aerodynamics and Flow Technology
German Aerospace Center (DLR)
Lilienthalplatz 7
38108 Braunschweig, Germany

ABSTRACT

Combustion noise in the laboratory scale PRECCINSTA burner is simulated with a new, robust and highly efficient approach for combustion noise prediction. The applied hybrid method FRPM-CN (Fast Random Particle Method for Combustion Noise prediction) relies on a stochastic, particle based sound source reconstruction approach. Turbulence statistics from reacting CFD-RANS simulations are used as input for the stochastic method, where turbulence is synthesized based on a first order Langevin ansatz. Sound propagation is modeled in the time domain with a modified set of linearized Euler equations and monopole sound sources are incorporated as right hand side forcing of the pressure equation at every timestep of the acoustics simulations. First, reacting steady state CFD simulations are compared to experimental data, showing very good agreement. Subsequently, the computational combustion acoustics setup is introduced, followed by comparisons of numerical with experimental pressure spectra. It is shown that FRPM-CN accurately captures absolute combustion noise levels without any artificial correction. Benchmark runs show that the computational costs of FRPM-CN are much lower than that of direct simulation approaches. The robustness and reliability of the method is demonstrated with parametric studies regarding source grid refinement, the choice of either RANS or URANS statistics and the employment of different global reaction mechanisms.

Nomenclature

Alphanumeric Variables

$\hat{A}$ Amplitude scaling variable of sources

The original publication is available at http://dx.doi.org/10.1115/1.4034236

a Thermal diffusivity, m^2/s

c Speed of sound, m/s

f Mixture fraction (CFD), frequency (CCA), Hz

$\mathcal{G}$ Gaussian filter kernel

h Heigth in the combustion chamber, mm

k Turbulent kinetic energy, $\mathrm{m}^2/\mathrm{s}^2$

l_T Turbulent (integral) lengthscale, m

$\dot{m}$ Mass flow rate, kg/s

P_{th} Thermal power, W

p Pressure, Pa

Q Source (general)

q_p Combustion noise source term, Pa/s

$\hat{R}$ Source variance for no separation

$\mathcal{R}$ Two-point correlation coefficient

r Vector of separation distance, mm

r Radial distance in the combustion chamber, mm

r_i Random value of particle i

s_i Random value, assigned to particle i

T Temperature, K

$\widetilde{T''^2}$ Temperature variance from CFD RANS, K^2

t Physical time, s

$\mathcal{U}$ Spatial white noise field

u Velocity vector, m/s

u_0^c Convection velocity from CFD RANS, m/s

V_S^n Source region, spatial dimension n

x Vector of spatial coordinates, mm

x' Noise component coordinates, mm

Greek Variables

β^* Turbulence model constant

γ Isentropic exponent

Δ Difference

δ Dirac delta function

ε Turbulent dissipation, $\mathrm{m}^2/\mathrm{s}^3$

μ Dynamic viscosity, $\mathrm{kg}/(\mathrm{ms})$

The original publication is available at http://dx.doi.org/10.1115/1.4034236

ξ Gaussian distributed noise forcing

ρ Density, kg/m^3

τ Time delay, s

τ_T Turbulent (integral) timescale, s

Φ Equivalence ratio

ω Turbulence frequency, $1/s$

φ Effectively realized source variance, Pa/s

Non-Dimensional Numbers

Ma Mach number; $\left(\frac{u}{c}\right)$

Pr Prandtl number; $\left(\frac{\mu}{\rho a}\right)$

Re Reynolds number; $\left(\frac{\rho u d}{\mu}\right)$

Mathematical Notations

$\dot{(...)}$ Rate of

$\widetilde{(...)}$ Favre-averaged quantity

$\overline{(...)}$ Reynolds-averaged quantity

$(...)'$ Fluctuating quantity

$(...)''$ Fluctuating quantity

$(...)^c$ Index for convection

$(...)^n$ Index of spatial dimension

$(...)_i$ Index for particle i

$(...)_{in}$ Index for inlet

$(...)_p$ Component in pressure equation

$(...)_T$ Related to turbulent temperature

$(...)_W$ Index for wall

$(...)_0$ Index for background flow field

$\langle ... \rangle$ Ensemble averaging

Acronyms and abbreviations widely used in text and list of references

CAA Computational Aero Acoustics

CCA Computational Combustion Acoustics

CFD Computational Fluid Dynamics

FRPM-CN Fast Random Particle Method for Combustion Noise Prediction

PIANO Perturbation Investigation of Aerodynamic Noise

PRECCINSTA Prediction and Control of Combustion Instabilities in Industrial Gas Turbines

RMS Root Meam Square

(U)RANS (Unsteady) Reynolds Averaged Navier Stokes

1 Introduction

Noise emission has become an issue with high social, environmental and economic relevance throughout the last years, especially in the field of aviation. The trend to more quiet aircrafts was already enforced in the early 2000s by for example the organisation ACARE (*Advisory Council for Aviation Research and Innovation in Europe*) with the formulation of noise emission targets until 2020 [1,2]. They postulate a reduction of overall levels by 50% compared to reference values of 2000. This goal still means a large discrepancy from today's status quo. However, ACARE goals were taken over in 2011 by a document of the European Comission, called FlightPath 2050 [3]. It extends existing ACARE goals to ambitious 65% up to 2050, relative to the year 2000. Considering those conditions, from today's point of view, there is a huge interest in fundamental research regarding noise sources and the design of noise reduction measures for aircrafts not only from regulative, political, but also from an industrial point of view.

Engine noise has the biggest contribution to overall noise levels in civil aircrafts [4–7]. The overall engine noise level itself contains several sources. Thus major noise contributions stem from the fan and turbine, which have broadband and tonal components as well as the compressor. Furthermore, there are contributions from the exhaust jet and the combustion chamber, both with mainly broadband character. Overall levels typically show a more or less broadband distribution, while the single subcomponents contribute at different frequency regimes [8]: Jet noise and combustion noise dominate at low frequencies, fan and turbine noise have significant amounts rather in the mid and high frequency regions.

From a phenomenological point of view, combustion noise can be subdivided into indirect and direct combustion noise. Indirect combustion noise is linked to convectively transported entropy spots and vorticity, while direct combustion noise is linked to mainly heat release flucutations in the reaction zones. The investigations in the presented paper focus on the modeling of the direct combustion noise phenomenon. Its relevance compared to the overall noise levels becomes more clear by looking at the recent developments of aircraft engines [9]: With the introduction of turbofan-engines, a significant reduction of jet noise was achieved by an exhaust nozzle exit velocity reduction, which resulted in larger bypass-ratios [10]. In the same turn, the introduction of turbofan engines led to a more significant contribution of fan noise to overall noise levels. On the other hand, in the past few decades, a large amount of research effort was put into the understanding of jet and fan noise and reduction measures as a consequence. This steadily led to an increased importance of combustion noise relative to the overall noise levels [8].

On the simulation side of combustion noise phenomena, alternatively to fully or partially scale resolving LES or DNS simulations, there are the so called hybrid approaches, separating CFD (Computational Fluid Dynamics) and CCA (Computational Combustion Acoustics [11]) scales. They provide a large potential for computational savings compared to direct simulations and the possibility to apply specifically optimized methods to each part of the problem [12], since acoustic pressure fluctuations are usually in the order of magnitude of the CFD computational error.

The original publication is available at http://dx.doi.org/10.1115/1.4034236

The particular line of development for the stochastic, particle based hybrid ansatz with correlated sources which is pursued here started with the introduction of the RPM (Random Particle Mesh Method) by Ewert and Emunds [13], while Ewert presented further extensions with applications to slat noise [14, 15], trailing edge and jet noise [16]. Their RPM realized sources with spatio-temporal correlations based on local turbulence statistics for the applications mentioned previously.

The approach of combustion noise modeling utilized in this work was derived by Mühlbauer et al. [17], using the sound source reconstruction algorithm from Ewert [13–16], while the derivation of the source term formulation was inspired by the cold jet noise model of Tam and Auriault [18]. The physical source term model was derived from first principles, using a fundamental pressure-density relation, leading to the linearized Euler energy equation with a right hand side forcing [19], while the complete right hand side source expression of the pressure-density relation was taken from Candel et al. [11]. The resulting formulation modeled with RPM was temperature variance based, while the variance field was determined by solving an additional transport equation according to Gerlinger [20] in the preceding CFD reacting RANS simulations. In a first approach to combustion noise prediction the RPM in conjunction with the acoustic perturbation equations (APEs) were used by Mühlbauer et al. [17]. The genuine APEs were introduced by Ewert and Schröder [21]. Later the source term model was reformulated on a more general basis, theoretically applicable to all reacting flow cases [22]. It was derived for the use in combination with the linearized Euler equations and the approach was called RPM-CN (Random Particle Mesh Method for Combustion Noise) [19, 22–25]. Mean flow field data and mean turbulence statistics for this causal approach were provided by steady-state RANS calculations, in view of potential computational savings compared to LES based methods.

On that basis, the method RPM-CN was advanced by Grimm et al. [26] by using the existing source term formulation but a different, highly efficient source reconstruction algorithm which is more suitable for technically relevant applications, the FRPM (Fast Random Particle Method) from Ewert et al. [27]. This approach, the so called FRPM-CN, was verified in terms of one- and two-point source statistics [26, 28, 29] as well as far-field spectra reproduction ability [28, 29] with an analytical framework introduced by Ewert et al. [30]. In the presented paper, the full dimensional model is validated for a laboratory combustor application case. The paper is structured as follows:

First, the theoretical framework of the combustion noise simulation approach including the sound source reconstruction algorithm is set. This is followed by a description of the investigated laboratory scale burner. Subsequently, the numerical CFD and CCA computational specifications are introduced. Consecutively, reacting CFD RANS simulations are validated with experimental data on lateral profile lines in the combustor. Parametric studies regarding the use of either RANS or URANS simulation mode, as well as the choice of different reaction schemes are carried out. Results are then used as an input for stochastic sound source reconstruction and sound propagation modeling in the following combustion acoustics simulations. Pressure spectra from the CCA simulations are compared to experimental data and simulation time is compared to a partially scale resolving, compressible simulation. It is shown that FRPM-CN is robust towards the use of different simulation input from CFD-RANS and combustion models. The hybrid method delivers absolute sound pressure levels of direct combustion noise at very low computational cost, compared to a compressible CFD method for a similar operation point.

2 Direct Combustion Noise Simulation

The main objective of this work is to apply a combustion noise monopole source term based model, which was originally formulated by Mühlbauer et al. [22], to a combustor application case. The basic underlying theory as well as the principle functioning of the sound source reconstruction algorithm, FRPM, which was combined with the combustion noise formulation by Grimm et al. [26, 28], is described in the following section.

2.1 Stochastic sound source reconstruction

The theory of the employed source reconstruction mechanism was presented in numerous publications, for example in [16, 19, 27] and will therefore only be briefly described.

FRPM generates statistically stationary, fluctuating sound sources $Q(x,t)$. A main requirement to the method is the accurate realization of one and two-point statistics of the resulting fluctuating field. The sound sources are constructed from an Eulerian point of view [23, 31]. The cross-covariance of the sources depends among others on the choice of spatial filtering and is - for the context of this work - Gaussian in space and exponential in time,

$$\begin{aligned}\mathcal{R}(x,r,\tau) &= \langle Q(x,t)Q(x+r,t+\tau)\rangle \\ &= \underbrace{\hat{A}(x)\hat{A}(x+r)l_T^n(x)}_{\hat{R}} \exp\left(-\frac{|\tau|}{\tau_T} - \frac{\pi|r-u_0^c\tau|^2}{4l_T^2(x)}\right).\end{aligned} \tag{1}$$

Equation (1) is the FRPM-method inherent correlation function and assumed to be approximately valid for the correlation function of monopole combustion noise sources in a turbulent flow regime. $\langle ...\rangle$ indicates ensemble averaging, l_T and τ_T denote integral length- and time scale and u_c is the convection velocity, accounting for Taylor's hypothesis. The convention with spatial variables is x for the source field location and r, the separation distance between sources. $\hat{R}$ denotes the variance of the correlated quantity for no separation space r and time τ.

The basic concept behind the employed reconstruction algorithm is to obtain fluctuating sound sources by the spatial filtering of a spatial white noise field $\mathcal{U}$,

$$Q(x,t) = \int_{V_S^n} \hat{A}(x)\,\mathcal{G}(|x-x'|,l_T)\,\mathcal{U}(x',t)d^n x'. \tag{2}$$

$\mathcal{G}$ represents the filtering operation, which is in the case of FRPM recursive [27, 32, 33]. It depends on x as well as the position x' of the respective noise component. The filter kernel width depends on the local length scale l_T. Integration is performed over the source domain V_S^n, n denotes the dimension. The amplitude function $\hat{A}$ needs to be scaled in a way that it realizes a local target variance for $Q(x,t)$ [19, 27, 34]. It is connected to the source variance $\hat{R}$ through

The original publication is available at http://dx.doi.org/10.1115/1.4034236

$$\hat{A} = \sqrt{\hat{R}(x)/l_T^n(x)}, \tag{3}$$

for $\mathcal{R}(x,0,0)$. The discrete interpretation of Eqn. (2) is the particle concept, where particles i at positions x_i carry a certain value, which is used for source reconstruction from filtering operations on a discrete spatial noise field.

Turbulence dynamics are modeled as follows: A decorrelation effect in time during particle convection is realized with an appropriate change of those values. This is induced through a Langevin equation [27, 35], which is shaped in a Lagrangian frame, reading

$$\frac{D_0}{Dt}\mathcal{U} = -\frac{1}{\tau_T}\mathcal{U} + \sqrt{\frac{2}{\tau_T}}\xi(x,t). \tag{4}$$

$D_0/Dt = \partial/\partial t + u_0^c \cdot \nabla$, where the convection velocity is determined by the averaged velocity field $u_0^c(x)$, which is extracted from RANS calculations. $\xi(x,t)$ represents spatio-temporal white noise with a Gaussian statistical distribution, for which the properties

$$\langle \xi(x,t) \rangle = 0, \tag{5}$$

$$\langle \xi(x,t)\xi(x+r,t+\tau) \rangle = \delta(\tau)\delta(r) \tag{6}$$

hold. Equation (4) and its implications to the properties of $\xi(x,t)$ and $\mathcal{U}$ account for the shape of the temporal part of the correlation function, Eqn. (1). Details on the employed concept of convective white noise and its impact on the properties of $\xi(x,t)$ and $\mathcal{U}$ are discussed in detail for example by Ewert et al. [27].

In Eqn. (2), a spatial filter is convoluted with the white noise field, leading to the spatial component of Eqn. (1), as shown for example in [23, 25]. The spatial filters used in this work have Gaussian shape, whereas the filter width is dependent on the local length scale, prescribed by the RANS flow field. The advancement of the random particle values in time and therefore the decorrelation mechanism is realized by discretizing Eqn. (4) according to

$$r_i(t+\Delta t) = \alpha r_i(t) + \beta s_i(t), \tag{7}$$

The original publication is available at http://dx.doi.org/10.1115/1.4034236

as explained in the literature [16, 25, 27]. A particle i carries a random value at time $t+\Delta t$, which is made up by $r_i(t)$ and $s_i(t)$ at time t, a Gaussian time-uncorrelated random value. This discrete approach realizes the exponential decay or decorrelation for the appropriate choice of α and β, which are both related to the time scale τ_s via $\alpha = 1-\Delta t/\tau_s$ and $\beta = (2\Delta t/\tau_s)^{1/2}$. β is chosen in a way to transiently preserve the RMS value of r_i.

2.2 Source term and acoustic model

The formulation of the employed combustion noise source model in conjunction with the linearized Euler equations was derived and presented in detail by Mühlbauer et al. [19]. A pressure-density relation with a generalized formulation for right-hand side (RHS) terms is reshaped so the left-hand side is equal to the energy equation of linearized Euler equations, expressed in terms of pressure, and an according RHS prescription rule is obtained. In the present work, a modified set of linearized Euler equations in combination with the existing source term formulation is used, since the genuine set of linearized Euler equations is prone to growing instabilities, especially in flow systems with large flow and density gradients, as present in combustion systems. Therefore, components with meanflow-gradient terms are neglected. This denotes a compromise for more stability of the computational combustion acoustics simulations but against an exact depiction of refraction effects [36]. As a consequence, a refraction error is induced. From our experience and a comparison of pressure signals of simulations with the full and reduced set of linearzed basic equations, almost no difference of time resolved pressure fluctuation in the combustion chamber could be observed. The modified set reads

$$\frac{\partial \rho'}{\partial t} + \widetilde{u}\cdot\nabla\rho' + \overline{\rho}\nabla\cdot u' = 0 \tag{8}$$

$$\frac{\partial u'}{\partial t} + (\widetilde{u}\cdot\nabla)\,u' + \frac{\nabla p'}{\overline{\rho}} = 0 \tag{9}$$

$$\frac{\partial p'}{\partial t} + \widetilde{u}\cdot\nabla p' + \gamma\overline{p}\nabla\cdot u' = q_p, \tag{10}$$

with the combustion noise source term

$$q_p = \frac{\gamma\overline{p}}{\widetilde{T}}\frac{\widetilde{D}T''}{Dt}. \tag{11}$$

$\gamma, \overline{p}$ and $\widetilde{T}$ are given as field variables from RANS calculations and they form the prefactor for the reconstructed combustion noise sources. The $\sim$ denotes Favre-averaging. The substantial time derivative $\widetilde{D}T''/Dt$ in Eqn. (11) is subject to (F)RPM reconstruction and therefore the variance and amplitude scaling according to Eqn. (1) and Eqn. (3) as well as the correlation function parameters in Eqn. (1), namely the turbulent length- and time-scale l_T and τ_T, have to be specified. The

The original publication is available at http://dx.doi.org/10.1115/1.4034236

variance scaling is formulated [19] for the temperature variance as the driving sound generation mechanism to

$$\hat{R} = \frac{\widetilde{T''^2}}{\tau_T^2} \quad \text{and} \quad \hat{A} = \frac{1}{\tau_T}\sqrt{\frac{\widetilde{T''^2}}{l_T^n}}, \tag{12}$$

according to Eqn. (3). The integral scales in Eqn. (12) are evaluated from CFD RANS field solutions from $l_T = \sqrt{k}/(\beta^*\omega)$ and $\tau_T = 1/(\beta^*\omega)$. The temperature variance, however, has to be determined from a transport equation [20, 25] in the preceding RANS calculations, reading

$$\begin{aligned}\frac{\partial \overline{\rho}\widetilde{T''^2}}{\partial t} + \frac{\partial \overline{\rho}\widetilde{u}_j\widetilde{T''^2}}{\partial x_j} &= \frac{\partial}{\partial x_j}\left\{\left(\overline{\mu} + \frac{\mu_t}{Pr_t}\right)\frac{\partial \rho\widetilde{T''^2}}{\partial x_j}\right\} \\ &+ c_{prod}\frac{\mu_t}{Pr_t}\left(\frac{\partial \widetilde{T}}{\partial x_j}\right)^2 - c_{diss}\overline{\rho}\frac{\overline{\varepsilon}}{\widetilde{k}}\widetilde{T''^2},\end{aligned} \tag{13}$$

with $c_{prod} = 2.0$ and $c_{diss} = 2.0$. It is solved as a postprocessing step and gives fairly good results in the carried out RANS calculations. The quality of the respective results will be evaluated in the context of the CFD validation studies of the subsequent sections.

3 The PRECCINSTA Burner

The numerically investigated PRECCINSTA (Prediction and Control of Combustion Instabilities in Industrial Gas Turbines) burner is schematically shown in Fig. 1. Presented validation studies are based on an experimental reference investigation of Dem et al. [37]. However, the validation of CFD studies in the framework of this paper focuses on technically premixed combustion. The burner works as follows:

An air plenum is mounted upstream of the burner. Air is led into the plenum and consecutively through a swirler into the combustion chamber. The radial swirler consists of 12 swirler channels. The fuel is induced from a fuel plenum into the swirler channels through single holes in a jet-in-crossflow arrangement [37]. Fuel and oxidizer then partially mix within a converging nozzle, which is characterized by a conical center body. The tip of the center body denotes the origin of the global coordinate system. Subsequently, the air-fuel mixture expands into the combustion chamber, which has the dimensions $85 \times 85 \times 114$mm. The burnt gas exits the combustion chamber through a converging nozzle. A detailed description of the experimental setup can be found in the literature [37]. The Reynolds number of the burner for a similar operation point was estimated to $\mathrm{Re} = 35,000$, based on a cold flow case at the combustor exit nozzle diameter [38]. The local Mach number at the combustor exit is estimated to $\mathrm{Ma} = 0.1$ and the maximum value is located in the nozzle prior to the combustion chamber expansion, amounting to about $\mathrm{Ma} = 0.15$.

The original publication is available at http://dx.doi.org/10.1115/1.4034236

Validation is carried out for the flow field with averaged results from particle image velocimetry (PIV) for the velocity components at horizontal profile lines in the combustion chamber at $h = 6\text{mm}, 10\text{mm}, 20\text{mm}, 40\text{mm}$, as shown in Fig. 2.
Single-shot laser Raman scattering measurements are available for temperature and temperature RMS profiles at the same positions for validation of combustion. Mean OH chemiluminescence and acoustic pressure measurements are available for a wide range of operation conditions. Acoustic fluctuating pressure is sampled at a combustion chamber reference microphone position at $x = 42.5\text{mm}, y = r = 42.5\text{mm}, z = h = 20\text{mm}$.
Since the numerical studies focus on the broadband combustion noise phenomenon, the selected operation condition is based on an acoustically relatively stable case at atmospheric conditions [39]. Air and fuel mass flow rates are $\dot{m}_{\text{air}} = 574\text{g/min}$ and $\dot{m}_{\text{fuel}} = 30\text{g/min}$ at the respective inlets, while the burner is operated at $P_{\text{th}} = 25\text{kW}$ and $\Phi = 0.9$ with a global mixture fraction of $f = 0.0498$. Methane and air is burnt in the previously described technically premixed configuration.

3.1 Numerical CFD Setup

The unstructured grid for the reacting CFD RANS simulations [40] is depicted in Fig. 3 by several intersecting planes through the combustor with local cell volume contours. The regions of the reaction zone as well as the swirler channels and the connecting ribs between air plenum and combustor are refined compared to the air plenum and downstream zones in the combustion chamber and the exhaust tube. The inner computational domain is entirely discretized with tetrahedra. Near wall regions in the swirler and combustion chamber are covered with three prism layers and they are interconnected to the inner domains via pyramid elements. The thetrahedral grid consists of 16.6M elements with 2.9M points. Furthermore, it consists of 0.47M prism elements and 5K pyramids. The grid is most refined in regions where fuel is injected to the swirler channels via thin tubes from the fuel plenum. Several configurations with different reaction mechanisms were tested on a finer grid, consisting of 22.8M elements. No significant differences in the numerical solution were observed. Therefore, presented results are from the coarser grid. The CFD simulations are conducted with the finite volume based DLR inhouse code THETA [41, 42]. It is based on the incompressible Navier-Stokes equations, treated with a SIMPLE (Semi-Implicit Method for Pressure Linked Equations) solution procedure. For the spatial discretization of the steady state RANS simulations, a first order accurate upwind scheme (UDS) is used. In case an URANS is performed, a second order accurate upwind (QUDS) scheme in space and a three point backward scheme (TPB) in time is chosen. The physical timestep in intermediate URANS simulations is $\Delta t = 1 \cdot 10^{-5}\text{s}$. For turbulence treatment, the $k\omega$-SST model in the formulation of Menter [43] is employed.
Mass flow is specified at air and fuel inlets with a turbulence degree of $\text{Tu} = 0.01$ and an initial turbulent lengthscale $l_T = 1 \cdot 10^{-4}\text{m}$ [44], respectively, at $T_{\text{in}} = 320\text{K}$. At the combustion chamber outlet tube, the static pressure is set to ambient reference conditions. Walls are treated as adiabatic except for isothermal combustion chamber walls, impinged with $T_{\text{W}} = 1500\text{K}$.
Monitoring positions of the mean flow field and combustion quantities are horizontal profile lines according to the respective PIV measurements at $h = 0.006\text{m}, 0.01\text{m}, 0.02\text{m}, 0.04\text{m}$. As a solution strategy, at first, steady state reacting simulations are carried out. In order to accurately predict chemical reactions, an intermediate URANS simulation with a physical timestep is attached in order to get a reasonable temperature field. This is in turn followed by another steady state RANS simulation,

the flow and combustion statistics of which are taken for the later CCA sound source reconstruction. Combustion is modeled with a combined EDM/FRC ansatz [45] for the treatment of global reaction schemes. A methane air mixture for combustion is investigated and two global reaction schemes are tested, a one-step mechanism proposed by Westbrook and Dryer [46] (WB1) and a five-step approach from Nicol et a. [47], while the formation of NOx is not considered. The mechanism from Nicol et al. is optimized with respect to flame speed (N5-DLR) and therefore denotes a modified version of the original set.

3.2 CCA specifications

CCA simulations are carried out with the DLR inhouse code PIANO (Perturbation Investigation of Aerodynamic Noise) [48]. PIANO is employed for sound propagation modeling via linearized Euler equations. Sound sources are reconstructed based on local turbulence statistics from CFD RANS simulations in FRPM (Fast Random Particle Method).

The computational grid for the acoustics simulations is shown in Fig. 4. The finite-difference based dispersion relation preserving Scheme (DRP) from Tam & Webb [49] is used for spatial discretization. The block-structured grid consists of 1.5M hexahedra with 1.94M nodes in 938 blocks. It spatially resolves frequencies up to $f_{\max} = 15$kHz. Experimental reference spectra are available up to 2kHz, therefore the computational combustion acoustics grid resolves a much larger wavenumber range than used for the comparison with experiments. However, the CCA grid resolution is determined by the geometry of the burner in combination with the use of a seven-point Finite Difference stencil.

For time progression, a four-step Runge Kutta scheme is used. The mesh is optimized with respect to the local growth rate of adjacent cells with a maximum growth rate in critical regions of 1.05. Those are zones with large velocity and density gradients close to the combustor inlet in the reaction zone or the swirler channels, where fuel is added to air in a jet-in-crossflow configuration. This optimization is needed for stability reasons, since rapidly changing velocity and density consequently means a locally changing speed of sound, which has to be appropriately resolved. Furthermore, accuracy of the Finite Difference scheme can only be approached with as much as possible regularly spaced grids.

Mean flow field quantities $\overline{\rho}, \tilde{u}, \tilde{v}, \tilde{w}, \overline{p}$ are interpolated from the unstructured CFD RANS grid to the CCA domain using a statistical Kriging [50] algorithm. The mean flow density field in the swirler channels is smoothed for stability reasons, to avoid large density gradients in adjacent cells due to the thin fuel jet.

The overall simulation time step is limited by the sound propagation modeling and depends on the grid size as well as the local Mach number according to $\Delta t_{\max} = (2.83\Delta x_{\min})/(\pi + \pi \mathrm{Ma})$. Therefore, a timestep of $\Delta t = 2.2 \cdot 10^{-7}$s is used. The cell determining the maximum time step is located in the combustor outlet tube, where a composition of hot combustion products is present.

The computational domain is enclosed by non-reflecting radiation boundary conditions [49] at the air plenum inlet tube, as shown in Fig. 4. An additional plenum is attached to the combustor outlet, which is in turn enclosed by a damping sponge layer and radiation conditions. Walls are modeled as fully reflecting, with the ghost point concept of Tam & Dong [51].

The spatial extension of the sound source region is determined from the discrete realization of Eqn. (11), which can be

interpreted as the effectively prescribed source target standard deviation,

$$\varphi = \frac{\gamma \overline{p}}{\tilde{T}} \sqrt{\frac{\widetilde{T''^2}}{\tau_T^2}}. \tag{14}$$

The field solution of Eqn. (14) from CFD RANS quantities is shown in Fig. 5, related to its field maximum value $\varphi/\varphi_{\max}$. As the main criterion for the determination of source field extensions, field values larger than 5% of the maximum value of φ are included. This leads to source field extensions of $x \in [-10\text{mm}; 50\text{mm}]$ and $y, z \in [-38\text{mm}; 38\text{mm}]$. Sources are reconstructed on an auxiliary equidistant and orthogonal grid. Two degrees of spatial discretization of the source domain are tested. The baseline resolution is $\Delta = 1\text{mm}$, which results in 346.6K cells and an initial distribution of random particles with 1.154 PPC (particles per cell). A finer grid configuration is tested with $\Delta = 0.655\text{mm}$ and resulting 1.2M cells with an initial particle distribution of 1.25 PPC. Particles are tracked in a Lagrangian frame, therefore the finer resolution results in significantly larger simulation turnaround times. As a consequence, it is desirable to obtain similar results from both discretizations in the CCA simulations, in order to be able to justify the choice of coarser source field resolution.

Sources are obtained from recursive filtering [32, 33] operations along the auxiliary grid, accounting for the local integral turbulent length scale. Turbulence is synthesized with a first order Langevin approach, as introduced with Eqns. (4) to (6), based on the local turbulent time scale. Integral one-point statistics are therefore extracted from the preceding CFD RANS simulations according to

$$l_T = \frac{\sqrt{k}}{\beta^* \omega} \quad \text{and} \quad \tau_T = \frac{1}{\beta^* \omega}, \tag{15}$$

with $\beta^* = 0.09$. A total of $N_{\text{CCA}} = 9 \cdot 10^5$ time steps is simulated, while resulting sound pressure spectra are evaluated over a time span of $\Delta t_{\text{overall}} = 0.2s$. Power spectral densities are evaluated from

$$S_{pp} = \lim_{t \to \infty} \left[\frac{\hat{p} \hat{p}^*}{t} \right], \tag{16}$$

where $\hat{p}$ is the Fourier transform of the pressure signal and $(...)^*$ indicates conjugate complex [52]. In the employed algorithm, the Wiener-Chintschin theorem is utilized, stating that the power spectral density is the Fourier transform of the autocorrelation of the signal. The narrowband spectrum with $\Delta f = 1\text{Hz}$ is then evaluated in accordance to the experiment from $10\text{lg}(S_{\text{pp}} \Delta f / p_{\text{ref}}^2)[\text{dB}]$.

Several configurations are tested for the CCA simulations, in order to demonstrate robustness of the method towards the choice of reaction mechanism, input of turbulence statistics, mean flow field, and source field resolution. The treated configurations are listed in Table 1.

4 CFD Results

The performance of employed CFD RANS models is evaluated by comparison of experimental flow field and temperature profiles along lateral measurement locations in the combustion chamber. Velocity profiles of RANS and URANS simulations with different global reaction schemes are compared in Fig. 6 and 7. There are certain common characteristics of the simulation profiles: The opening angle of the swirl flow while entering the combustion chamber is accurately reproduced consistently throughout all simulations, regardless of the use of either RANS or URANS mode. Furthermore, the swirl strength, herein indicated with the depiction of radial velocity profiles in Fig. 7, is nicely reproduced in the simulations, not only in terms of spatial distribution, but also for absolute velocity values. A noticeable difference between RANS and URANS simulations becomes clear from Fig. 6: The second order accurate spatial discretization scheme used for the URANS simulations gives a significantly better representation of peak values in the axial velocity profiles than the more diffusive first order accurate RANS discretization. Therefore, in the context of the CCA parametric studies, the use of either RANS or URANS velocity fields means an investigation of the influence of different source convection velocity on shape and levels of sound pressure spectra. However, shape and absolute velocity values in the inner recirculation zone around the burner axis are almost exactly and consistently reproduced.

In terms of comparison of temperature and temperature RMS profiles, either RANS and URANS simulations deliver good agreement with experimental data. Profile lines of mean temperature are shown in Fig. 8. For this particular operation point, the flame anchors at the tip of the conical center body in the convergent nozzle and therefore in the inner recirculation zone. Compared to RANS simulations, the URANS shows slightly better performance in the outer recirculation zones, concerning the match of temperature levels with experimental data. The same circumstance can be observed for the outer peaks of temperature RMS profiles in Fig. 9. Only modeled fluctuations are shown for all cases, since resolved fluctuations in URANS simulations of this particular case are negligible.

In general, peak temperature levels are overpredicted in the numerical simulation, presumably due to the use of simplified global reaction schemes. However, the five-step formulation from Nicol et al. performs slightly better than the one-step scheme proposed by Westbrook and Dryer, as expected. Further on, the simulations with the Nicol five-step mechanism gives better agreement with experimental data regaring peak values of temperature variance profiles.

In summary, the presented CFD (U)RANS simulations provide acceptable representations of flow field and combustion of the treated operation point. Previously discussed differences that were linked to the respective models and their impact on resulting pressure spectra are discussed in the following section.

5 Combustion Acoustics Results

Fig. 10 shows slices through the combustor with contours of instantaneous acoustic pressure in the CCA domain as well as a contour of mean temperature distribution on the CFD RANS computational domain. Shape and distribution of direct combustion noise sources are indicated via exemplary iso-surfaces. No spurious reflections on radiation boundary conditions at inlet tube and outlet plenum are observed, the respective boundaries act as non-reflecting surfaces. The peak fluctuations of acoustic pressure usually occur close to the combustor front plate, in the burner nozzle and the swirler channels. As becomes

The original publication is available at http://dx.doi.org/10.1115/1.4034236

clear from looking at the CFD temperature distribution in the combustion chamber, the direct combustion noise sources are mainly located in the inner shear layer between main air-fuel stream and inner recirculation zone, where the main reaction zone is located.

Fig. 11 displays a comparison of measured spectra [53] with parametric studies from the computational combustion acoustics simulations with FRPM-CN. Acoustic pressure measurements were carried out with sound-hard metal walls and also with glass walls for optical access, which are loosely mounted in order to avoid large thermally induced stresses. The latter configuration induces a certain broadband damping effect. FRPM-CN simulations are compared to both, in order to get consistency with combustion chamber wall boundary conditions between experiment and simulation.

The difference between technical (TP) and perfect (PP) premixing is that in the technical premixing case, fuel is induced through the fuel plenum into the swirler channels, while for perfect premixing, a homogeneous air fuel mixture is induced into the upstream air plenum and the fuel plenum has no functionality. As can be seen in Fig. 11, the two cases of premixing (red and green curve) show a similar acoustical behaviour. The comparison between technically and perfectly premixed configurations is incorporated due to the lack of measurement data with sound hard walls of the technically premixed case. The damping effect induced by the glass walls in the technically premixed case however seems likely to be similar to the herein shown effect of the perfectly premixed configuration (green and blue curve).

For the considered configuration, the use of sound hard walls in the experiment induces a frequency-dependent shift of amplitudes towards higher values. The comparison of the two configurations in the experiment disclosed that the originally considered stable case [39] turns out to be highly unstable when using sound hard walls. However, the fraction of turbulent combustion noise in the measured spectrum (blue curve) in Fig. 11 is met by FRPM-CN.

Parametric studies regarding a variation of turbulence modeling (RANS/URANS), the employment of different reaction mechanisms (N5-DLR/WB1) or a different degree of resolution of the source field have no significant impact on the pressure spectra. Therefore, it can be stated that FRPM-CN is robust and reliable towards the choice of different submodels. Furthermore, differences in the realization of source convection velocity (RANS/URANS), as discussed in the CFD results section, do not significantly influence the respective pressure spectra.

Simulations with FRPM-CN reproduce sound pressure levels well, especially in the low frequency regime for measured sound hard wall boundary conditions. The numerical simulations furthermore accurately reproduce the slope of spectra in the mid- and high-frequency regimes. Thus, absolute amplitudes are captured well over most parts of the experimental spectrum.

However, the hybrid approach cannot depict the thermoacoustic instabilities indicated by the 400Hz and 800Hz peaks, which are due to a Helmholtz mode and its first harmonic. The sequential method does not account for feedback effects from acoustics back to flow field and combustion and therefore gives the fraction of noise that is produced from turbulent combustion noise sources.

The simulations were carried out in a total of 4052 CPU-h, while the CFD fraction of computational time amounts to 1356 CPU-h. For comparison with a scale adaptive simulation (SAS) of this particular burner, the operation point $P_{\text{th}} = 25.1\text{kW}$ and $\Phi = 0.7$ was investigated. The computation was done with the DLR-inhouse code THETA and the fractional step solver

SICS [54], which enables the treatment of compressible flows and therefore the capturing of acoustics. Detailed specifications of the simulation can be found in the literature [55]. Simulations were conducted on 256 cores in 11 days on an unstructured 44M-cell grid and therefore in 67584 CPU-h in total for the simulation of six mean combustor flow through times or 60ms [55]. FRPM-CN simulation real-time for the evaluation of pressure spectra in the herein treated case is 0.2s. An equal simulation for this realtime with the partially scale resolving method would add up to 225300 CPU-h. Accounting for this, FRPM-CN is faster by a factor of approximately 55.6.

6 Conclusions

A hybrid, particle based approach for combustion noise prediction was applied and validated for a model combustor. The method relies on turbulence statistics and mean flow field quantities derived from preceding CFD RANS simulations. Stochastic sound source reconstruction and sound propagation was done in the time domain. The presented study focused on the turbulent combustion noise phenomenon in a low Mach number, swirl stabilized combustor.

RANS and URANS simulations were carried out with slightly different output of flow field and combustion. On that basis, parametric studies were performed to test the sensitivity of FRPM-CN for variations in flow field, turbulence statistics and temperature profiles and the impact on resulting sound pressure spectra. Furthermore, a change in the degree of source field discretization was tested. A modified set of linearized Euler equations was employed for sound propagation modeling, accounting for a steady state background flow field. The modified set denotes a compromise for stability of the simulation but against an exact depiction of refraction effects. The genuine linearized Euler equations are capable of tracking modes linked to entropy or vorticity. However, in the present low Mach number testcase, indirect combustion noise phenomena are assumed to be of minor importance, which was confirmed by good agreement between measured and calculated pressure spectra.

It was found that the investigated parametric changes did not significantly influence the spectral outcome of the method and absolute sound pressure levels were accurately captured at very low computational costs, especially compared to direct compressible simulation approaches. Reliability of the method was demonstrated in the presented investigations. Therefore, FRPM-CN is highly attractive for technically relevant applications in an industrial environment but also for fundamental investigations in question of noise sources and sound propagation in complex combustion systems.

Acknowledgements

Dr. Michael Stöhr and Stefanie Werner from the DLR Institute of Combustion Technology are gratefully acknowledged for the provision of their experimental data on pressure spectra.

References

[1] ACARE, 2001. “Strategic research agenda, volume 1”. www.acare4europe.org.

[2] European Comission, 2001. “European aeronautics: A vision for 2020”. Office for Official Publications of the European Communities, Luxembourg, ISBN 92-894-0559-7.

[3] European Comission, 2011. “Flightpath 2050: Europe’s vision for aviation”. Office for Official Publications of the European Communities, Luxembourg, ISBN 978-92-79-19724-6, doi 10.2777/5026.

[4] Rolls-Royce, 1996. *The Jet Engine*. Technical Publications Department, Rolls-Royce plc, Derby, England. ISBN 10: 0902121235.

[5] Deane, E., 2009. “Use of fan rig data for the understanding and prediction of fan broadband noise and noise changes due to a variable area nozzle”. Dissertation, Institute of Sound and Vibration Research, Faculty of Engineering, Science and Mathematics, University of Southampton.

[6] Leylekian, L., Lebrun, M., and Lempereur, P. “An overview of aircraft noise reduction technologies”. *Aerospace Lab Journal*.

[7] Airbus, 2003. “Getting to grips with aircraft noise”.

[8] Dowling, A., and Mahmoudi, Y., 2015. “Combustion noise”. *Proceedings of the Combustion Institute,* **35**, pp. 65–100.

[9] Duran, I., Moreau, S., Nicoud, F., Livebardon, T., Bouty, E., and Poinsot, T. “Combustion noise in modern aero-engines”. *Aerospace Lab Journal,* **7**.

[10] Lighthill, M. “On sound generated aerodynamically. i. general theory”. *Proceedings of the Royal Society*.

[11] Candel, S., Durox, D., Ducruix, S., Birbaud, A.-L., Noiray, N., and Schuller, T., 2009. “Flame dynamics and combustion noise: progress and challenges”. *International Journal of Aeroacoustics,* **8**(1), pp. 1–56.

[12] Bui, T., Schröder, W., and Meinke, M., 2008. “Numerical analysis of the acoustic field of reacting flows via acoustic perturbation equations”. *Computers & Fluids,* **37**(9), pp. 1157–1169.

[13] Ewert, R., and Emunds, R., 2005. “CAA Slat Noise Studies Applying Stochastic Sound Sources Based On Solenoidal Digital Filters”. In 11th AIAA/CEAS Aeroacoustics Conference, AIAA 2005-2862.

[14] Ewert, R., 2006. “Slat Noise Trend Predictions Using CAA With Stochastic Sound Sources From A Random Particle-Mesh Method (RPM)”. In 12th AIAA/CEAS Aeroacoustics Conference, AIAA 2006-2667.

[15] Ewert, R., 2008. “Broadband Slat Noise Prediction Based on CAA and Stochasic Sound Sources from a Fast Random Particle-Mesh (RPM) Method”. *Computers and Fluids Journal,* **37**(4), pp. 369–387.

[16] Ewert, R., 2007. “RPM - the fast random particle-mesh method to realize unsteady turbulent sound sources and velocity fields for CAA applications”. In 13th AIAA/CEAS Aeroacoustics Conference, AIAA 2007-3506.

[17] Mühlbauer, B., Ewert, R., Kornow, O., Noll, B., Delfs, J., and Aigner, M., 2008. “Simulation of combustion noise using CAA with stochastic sound sources from RANS”. In 14th AIAA/CEAS Aeroacoustic Conference. AIAA 2008-2944.

[18] Tam, C., and Auriault, L., 1999. “Jet Mixing Noise from Fine-Scale Turbulence”. *AIAA Journal,* **37**(2), pp. 145–153.

[19] Mühlbauer, B., Ewert, R., Kornow, O., and Noll, B., 2010. “Evaluation of the RPM Approach for the Simulation of Broadband Combustion Noise”. *AIAA Journal,* **48**(7), pp. 1379–1390.

[20] Gerlinger, P., 2005. *Numerische Verbrennungssimulation - Effiziente Numerische Simulation turbulenter Verbrennung*. Springer-Verlag, Germany. ISBN 3-540-23337-7.

[21] Ewert, R., and Schröder, W., 2003. "Acoustic perturbation equations based on flow decomposition via source filtering". *Journal of Computational Physics,* **188**, pp. 365–398.

[22] Mühlbauer, B., Ewert, R., Kornow, O., Boyde, J., Noll, B., Delfs, J., and Aigner, M., 2009. "Evaluation of the RPM-CN approach for broadband combustion noise prediction". In 15th AIAA/CEAS Aeroacoustic Conference. AIAA 2009-3285.

[23] Mühlbauer, B., Ewert, R., Kornow, O., Noll, B., and Aigner, M., 2009. "Numerical simulation of broadband combustion noise with the RPM-CN approach". In Proceedings of ASME Turbo Expo 2009. GT2009-59870.

[24] Mühlbauer, B., Ewert, R., Kornow, O., and Noll, B., 2012. "Broadband combustion noise simulation of open non-premixed turbulent jet flames". *International Journal of Aeroacoustics,* **11**(1), pp. 1–24.

[25] Mühlbauer, B., 2012. "Numerische Simulation von Verbrennungslärm". Dissertation, Institut für Verbrennungstechnik der Luft- und Raumfahrt, Universität Stuttgart. http://elib.uni-stuttgart.de/opus/volltexte/2012/7137/.

[26] Grimm, F., Ewert, R., Dierke, J., Noll, B., and Aigner, M., 2014. "Broadband combustion noise prediction with the fast random particle method". In Proceedings of ASME Turbo Expo 2014. GT2014-25195.

[27] Ewert, R., Dierke, J., Siebert, J., Neifeld, A., Appel, C., Siefert, M., and Kornow, O., 2011. "CAA broadband noise prediction for aeroacoustic design". *Journal of Sound and Vibration,* **330**(17), pp. 4139–4160.

[28] Grimm, F., Ewert, R., Dierke, J., Noll, B., and Aigner, M., 2014. "The fast random particle method for combustion noise prediction". In 20th AIAA/CEAS Aeroacoustics Conference. AIAA Paper 2014-2451.

[29] Grimm, F., Ewert, R., Dierke, J., Noll, B., and Aigner, M., 2015. "Efficient full 3D turbulent combustion noise simulation based on stochastic sound sources". In 21st AIAA/CEAS Aeroacoustics Conference. AIAA Paper 2015-2973.

[30] Ewert, R., Neifeld, A., and Fritzsch, A., 2011. "A 3-D modal stochastic jet noise source model". In 17th AIAA/CEAS Aeroacoustics Conference. AIAA Paper 2011-2887.

[31] Mühlbauer, B., Ewert, R., Kornow, O., Noll, B., Delfs, J., and Aigner, M., 2009. "Numerical simulation of broadband combustion noise based on stochastic source reconstruction". In 16th International Congress on Sound and Vibration. Krakow, Poland.

[32] Purser, R., Wu, W.-S., Parrish, D., and Roberts, N., 2003. "Numerical aspects of the application of recursive filters to variational statistical analysis. part i: Spatially homogeneous and isotropic gaussian covariances". *Monthly Weather Review,* **131**, pp. 1524–1535.

[33] Purser, R., Wu, W.-S., Parrish, D., and Roberts, N., 2003. "Numerical aspects of the application of recursive filters to variational statistical analysis. part ii: Spatially inhomogeneous and anisotropic gaussian covariances". *Monthly Weather Review,* **131**, pp. 1536–1548.

[34] Ewert, R., Dierke, J., Pott-Pollenske, M., Appel, C., Emunds, R., and Sutcliffe, M., 2010. "CAA-RPM prediction and validation of slat setting influence on broadband high-lift noise generation". In 16th AIAA/CEAS Aeroacoustics

Conference, AIAA 2010-3833.

[35] Pope, S., 2000. *Turbulent Flows*. Cambridge University Press, UK. ISBN 0-521-59886-9.

[36] Ewert, R., Kornow, O., Delfs, J., Yin, J., Röber, T., and Rose, M., 2009. "A CAA Based Approach to Tone Haystacking". In 15th AIAA/CEAS Aeroacoustics Conference, AIAA 2009-3217.

[37] Dem, C., Stöhr, M., Arndt, C., Steinberg, A., and Meier, W. "Experimental study of turbulence-chemistry interactions in confined swirl flames with different degrees of premixing". *Zeitschrift für Physikalische Chemie*.

[38] Meier, W., Weigand, P., Duan, X., and Giezendanner-Thoben, R., 2007. "Detailed characterization of the dynamics of thermoacoustic pulsations in a lean premixed swirl flame". *Combustion and Flame,* **150**, pp. 2–26.

[39] Grimm, F., Ohno, D., Werner, S., Stöhr, M., Ewert, R., Dierke, J., Noll, B., and Aigner, M., 2016. "Direct combustion noise simulation of a lean premixed swirl flame using stochastic sound sources". In 54th AIAA Aerospace Sciences Meeting. AIAA Paper 2016-1881.

[40] Domenico, M. D., 2015. "Private communication".

[41] Domenico, M. D., Gerlinger, P., and Noll, B., 2011. "Numerical simulations of confined, turbulent, lean, premixed flames using a detailed chemistry combustion model". In Proceedings of the ASME Turbo Expo 2011. GT2011-45520.

[42] Reichling, G., Noll, B., and Aigner, M., 2013. "Development of a Projection-Based Method for the Numerical Calculation of Compressible Reactive Flows". In Proceedings of the 51st AIAA Aerospace Sciences Meeting including the New Horizons Forum and Aerospace Exposition. AIAA 2013-1003.

[43] Menter, F., Kuntz, M., and Langtry, R., 2003. "Ten Years of Industrial Experience with the SST Turbulence Model". *Turbulence, Heat and Mass Transfer 4, ed: K. Hanjalic, Y. Nagano, and M. Tummers, Begell House, Inc.*, pp. 625–632.

[44] Lourier, J.-M., Noll, B., and Aigner, M., 2014. "Large eddy simulation of a thermoacoustic instability within a swirl-stabilized burner using impedance boundary conditions". In Proceedings of ASME Turbo Expo 2014. GT2014-26200.

[45] Reichling, G., Noll, B., and Aigner, M., 2013. "Numerical simulation of the non-reactive and reactive flow in a swirled model gas turbine combustor". In 21st AIAA Computational Fluid Dynamics Conference. AIAA 2013-2434.

[46] Westbrook, C., and Dryer, F., 1981. "Simplified reaction mechanisms for the oxidation of hydrocarbon fuels in flames". *Combustion Science and Technology,* **27**, pp. 31–43.

[47] Nicol, D., Malte, P., Hamer, A., Roby, R., and Steele, R., 1999. "Development of a five-step global methane oxidation-no formation mechanism for lean-premixed gas turbine combustion". *J. Eng. Gas. Turb. Power,* **121**(2), pp. 272–280.

[48] Delfs, J., Bauer, M., Ewert, R., Grogger, H., Lummer, M., and Lauke, T., 2008. *Numerical Simulation of Aerodynamic Noise with DLR's aeroacoustic code PIANO*, 5.2 ed. DLR - German Aerospace Center, Braunschweig, Germany.

[49] Tam, C., and Webb, J., 1993. "Dispersion-Relation-Preserving Finite Difference Schemes for Computational Acoustics". *Journal of Computational Physics,* **107**(2), pp. 262–281.

[50] Krige, D., 1951. "A statistical approach to some basic mine valuation problems on the witwatersrand". *J. of the Chem., Metal and Mining Soc. of South Africa,* **52**(6), pp. 119–139.

[51] Tam, C., and Dong, Z., 1994. "Wall boundary conditions for high-order finite-difference schemes in computational

aeroacoustics". *Theoret. Comput. Fluid Dynamics,* **6**, pp. 303–322.

[52] Ewert, R., Appel, C., Dierke, J., and Herr, M., 2009. "RANS/CAA based prediction of NACA 0012 broadband trailing edge noise and experimental validation". In 15th AIAA/CEAS Aeroacoustics Conference, AIAA 2009-3269.

[53] Stöhr, M., and Werner, S., 2015. *Private communication*.

[54] Lourier, J.-M., Noll, B., and Aigner, M., 2013. "Extension of a compressible pressure-based solver for reacting flows". In 19th AIAA/CEAS Aeroacoustics Conference. AIAA 2013-2101.

[55] Lourier, J.-M., Eberle, C., Noll, B., and Aigner, M., 2015. "Influence of turbulence-chemistry interaction modeling on the structure and the stability of a swirl-stabilized flame". In Proceedings of ASME Turbo Expo 2015. GT2015-43174.

The original publication is available at http://dx.doi.org/10.1115/1.4034236

List of Tables

List of Figures

The original publication is available at http://dx.doi.org/10.1115/1.4034236

Table 1: List of configurations for CCA simulations

Case	Sim. mode	Reaction scheme	Source field res.
1	RANS	N5-DLR	coarse
2	RANS	WB1	coarse
3	RANS	N5-DLR	fine
4	URANS	N5-DLR	coarse
5	URANS	WB1	coarse

The original publication is available at http://dx.doi.org/10.1115/1.4034236

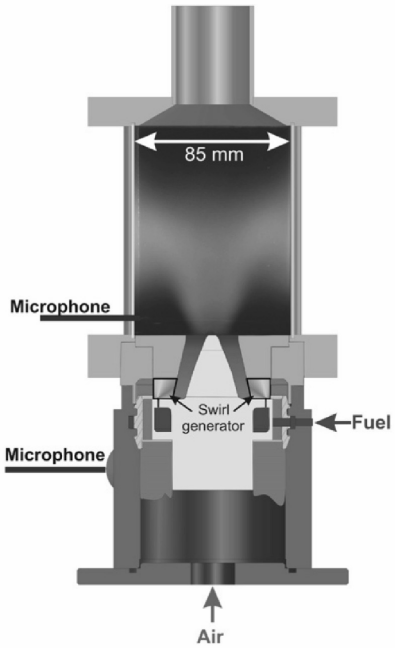

Fig. 1: Schematic drawing of the PRECCINSTA burner with exemplary flame structure and basic dimensions [37]

The original publication is available at http://dx.doi.org/10.1115/1.4034236

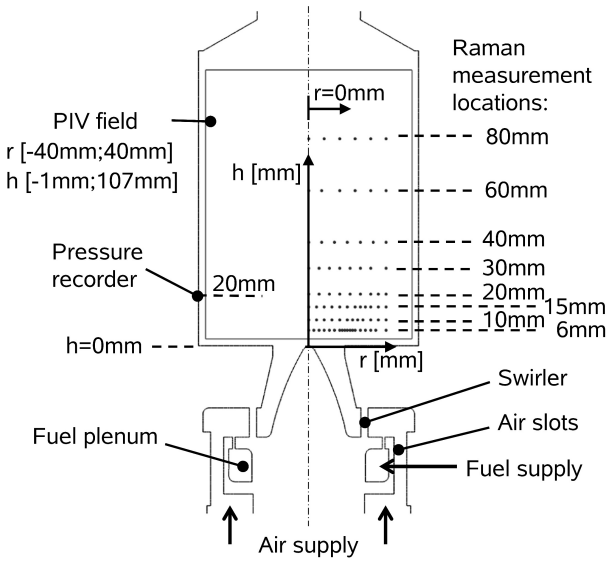

Fig. 2: Dimensions of PIV, Raman and acoustic pressure measurements for validation studies in the PRECCINSTA burner

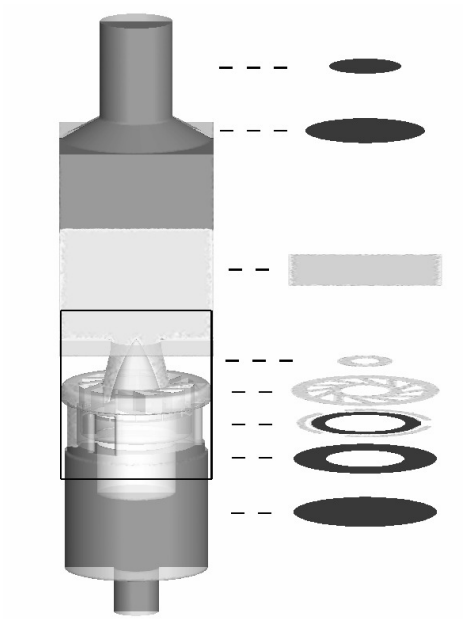

Fig. 3: CFD computational domain of the PRECCINSTA burner with local cell volume on intersecting planes. Highlighted swirler and air-fuel mixing region. Bright color indicates $V_{\text{cell}} = 1 \cdot 10^{-10}\text{m}^3$, dark color $V_{\text{cell}} = 3.5 \cdot 10^{-11}\text{m}^3$

The original publication is available at http://dx.doi.org/10.1115/1.4034236

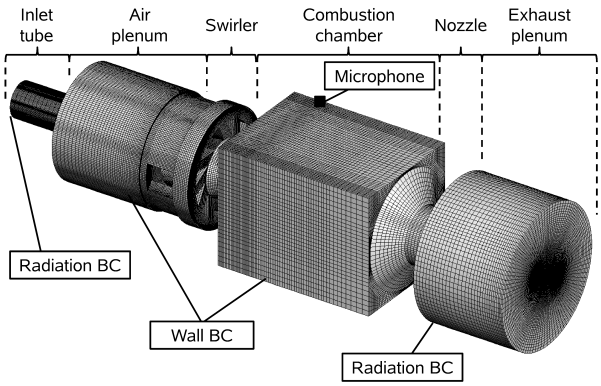

Fig. 4: Block-structured mesh for the computational combustion acoustics simulations with employed boundary conditions

The original publication is available at http://dx.doi.org/10.1115/1.4034236

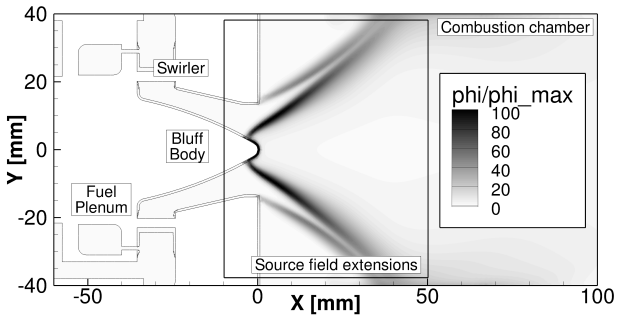

Fig. 5: Discrete realization of effective source standard deviation from CFD-RANS quantities with chosen source field extensions, depicted on the CFD computational domain

The original publication is available at http://dx.doi.org/10.1115/1.4034236

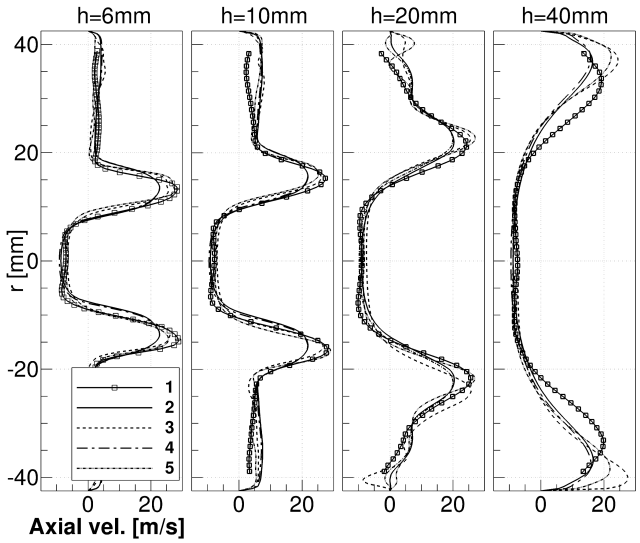

Fig. 6: Comparison of axial velocity of different simulation configurations with experimental data on lateral profile lines. 1: PIV measurements, 2: RANS, N5-DLR reaction mechanism, 3: URANS, N5-DLR reaction mechanism, 4: RANS, WB1 reaction mechanism, 5: URANS, WB1 reaction mechanism

The original publication is available at http://dx.doi.org/10.1115/1.4034236

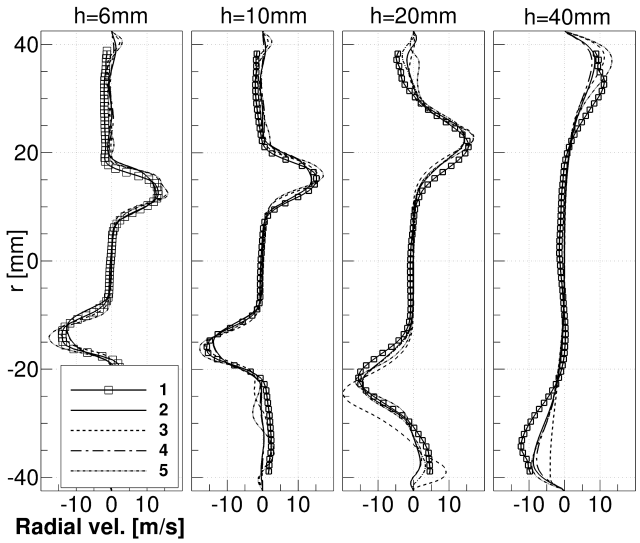

Fig. 7: Comparison of radial velocity of different simulation configurations with experimental data on lateral profile lines. 1: PIV measurements, 2: RANS, N5-DLR reaction mechanism, 3: URANS, N5-DLR reaction mechanism, 4: RANS, WB1 reaction mechanism, 5: URANS, WB1 reaction mechanism

The original publication is available at http://dx.doi.org/10.1115/1.4034236

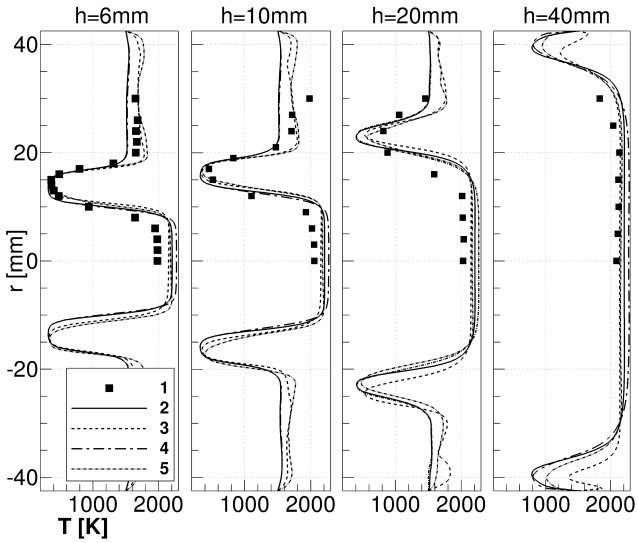

Fig. 8: Comparison of temperature of different simulation configurations with experimental data on lateral profile lines. 1: Raman measurements, 2: RANS, N5-DLR reaction mechanism, 3: URANS, N5-DLR reaction mechanism, 4: RANS, WB1 reaction mechanism, 5: URANS, WB1 reaction mechanism

The original publication is available at http://dx.doi.org/10.1115/1.4034236

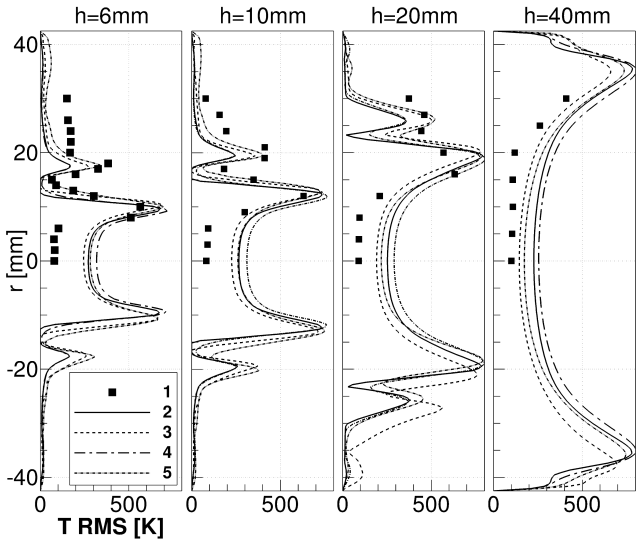

Fig. 9: Comparison of temperature RMS of different simulation configurations with experimental data on lateral profile lines. 1: Raman measurements, 2: RANS, N5-DLR reaction mechanism, 3: URANS, N5-DLR reaction mechanism, 4: RANS, WB1 reaction mechanism, 5: URANS, WB1 reaction mechanism

The original publication is available at http://dx.doi.org/10.1115/1.4034236

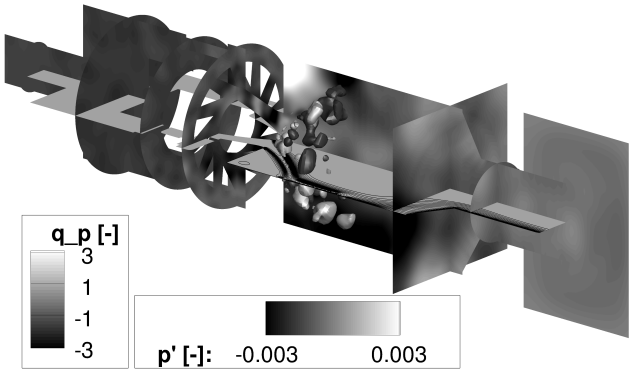

Fig. 10: CFD computational domain with midplane distribution of temperature, lateral surfaces with instantaneous acoustic pressure fluctuation and isosurfaces of the combustion noise source term. Quantities of acoustics simulations referenced to air plenum atmospheric conditions, $q_p = q_p/(f\rho c^2)$ and $p' = p'/(\rho c^2)$

The original publication is available at http://dx.doi.org/10.1115/1.4034236

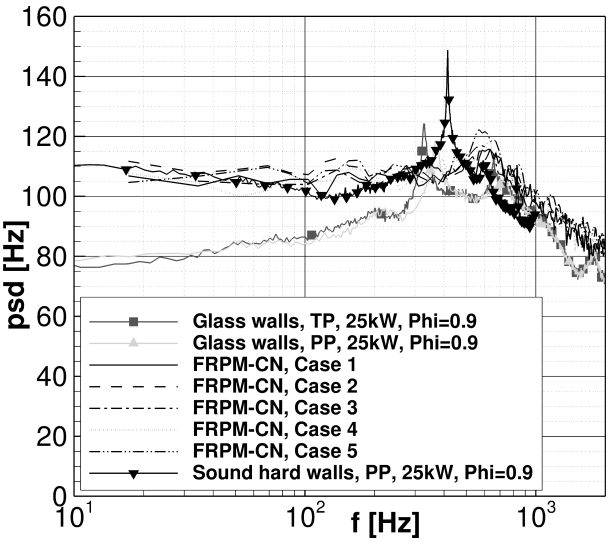

Fig. 11: Power spectral density of experimental sound pressure and FRPM-CN parametric studies. Simulation cases according to Table 1. TP: Technically premixed, PP: Perfectly premixed

The original publication is available at http://dx.doi.org/10.1115/1.4034236